

# JGR Space Physics



## DATA ARTICLE

10.1029/2022JA031254

## The Cluster Virtual Observatory for ULF Waves

O. D. Constantinescu<sup>1,2</sup> , K. H. Fornaçon<sup>1</sup>, U. Motschmann<sup>3</sup>, K. H. Glassmeier<sup>1</sup> , I. Richter<sup>1</sup> , and F. Plaschke<sup>1</sup>

### Key Points:

- The Cluster Virtual Observatory (CVO) is an on-line archive of low frequency wave parameters based on Cluster measurements
- The CVO also provides the tetrahedron geometrical configuration parameters
- The waves and configuration parameters are available as quick-plots as well as binary *Hierarchical Data Format* data

### Supporting Information:

Supporting Information may be found in the online version of this article.

### Correspondence to:

O. D. Constantinescu,  
[d.constantinescu@tu-bs.de](mailto:d.constantinescu@tu-bs.de)

### Citation:

Constantinescu, O. D., Fornaçon, K. H., Motschmann, U., Glassmeier, K. H., Richter, I., & Plaschke, F. (2023). The Cluster Virtual Observatory for ULF waves. *Journal of Geophysical Research: Space Physics*, 128, e2022JA031254. <https://doi.org/10.1029/2022JA031254>

Received 22 DEC 2022

Accepted 22 AUG 2023

<sup>1</sup>Institute for Geophysics and Extraterrestrial Physics, Technische Universität Braunschweig, Braunschweig, Germany,

<sup>2</sup>Institute for Space Sciences, Bucharest, Romania, <sup>3</sup>Institute for Theoretical Physics, Technische Universität Braunschweig, Braunschweig, Germany

**Abstract** Since its launch in 2000, the Cluster fleet visited a vast domain of the circum-terrestrial environment, from the upstream solar wind and the distant tail, down to the plasmasphere, scanning in detail all magnetospheric regions during over two solar cycles. This led to an unprecedentedly rich data collection of multi-point measurements which will be used for years to come to decipher the mechanisms of Solar-Terrestrial interactions. The large volume of data gathered by Cluster requires special strategies to make efficient use of it. To address this issue we constructed a browsable database containing parameters of the detected Ultra low frequency waves and of the spacecraft formation geometry. The primary data used to derive the parameters are the magnetic field, the electric field and the electron density. The data is resampled to a cadence of 1 s and processed using a sliding analysis window of 2,048 s with a step of 256 s over 24 hr intervals. This results in time-frequency arrays for each parameter covering the 0.5 mHz to 0.5 Hz frequency range. The database is accessible at <http://plasma.space-science.ro/cluster.html>. In total there are 47 wave parameters in the database, among them being the ellipticity, the degree of polarization, the (unsigned) wave vector direction, and the Poynting vector. Plots for the planarity, elongation, and degeneration of the Cluster tetrahedron are also available. At the moment, the database covers measurements made between 01 January 2001 and 31 December 2020 with more data being added in time. Here we present this database, discuss the methods used to derive the parameters and give practical examples.

**Plain Language Summary** This work describe an on-line database containing data and plots of physical quantities characterizing low frequency waves detected by the Cluster spacecraft fleet in the space plasma around the Earth. These quantities are derived using measurements of the magnetic field, electric field, and particles taken by the four spacecraft over 20 years. The plots can be used to quickly assess the plasma waves activity over a certain time interval, while the data can be used for further analysis.

## 1. Introduction

The Cluster mission (Escoubet et al., 1997), consisting of four identical spacecraft flying in formation around the Earth, is the first multi-spacecraft mission to study the Earth's magnetosphere and the near Earth solar wind. Simultaneous measurements allowed for the first time to separate spatial from temporal fluctuations and to investigate the three-dimensional structures in the Earth's plasma environment. Each spacecraft carries 11 state-of-the-art instruments to measure the surrounding plasma properties. One of the key quantities delivered is the magnetic field which is measured by two instruments: a searching coil magnetometer (Cornilleau-Wehrin et al., 1997) measures the high frequency fluctuations of the magnetic field and a flux gate magnetometer (FGM) (Balogh et al., 1997) measures the low frequency fluctuations. The spacecraft were launched in July and August 2000 on polar orbits and they will likely deliver science data at least until 2024 when the first spacecraft in the formation enters the Earth's upper atmosphere (Lemmens et al., 2017).

Ultra low frequency (ULF) waves are oscillations of the electromagnetic field occurring in the magnetized plasma around the Earth at frequencies in the order of mHz to Hz (Glassmeier, 1995; Keiling et al., 2016; Pilipenko, 1990). They play a crucial role in the transfer and distribution of the energy coming from the Sun by energizing particles, triggering reconnection, storing and propagating energy, modifying distribution functions, and carrying information between distant regions of the magnetosphere and the solar wind. Various wave modes are excited, depending on the local plasma parameters as well as on the solar wind conditions, and each wave mode has its particular way of interacting with the magnetosphere.

© 2023. The Authors.

This is an open access article under the terms of the [Creative Commons Attribution License](https://creativecommons.org/licenses/by/4.0/), which permits use, distribution and reproduction in any medium, provided the original work is properly cited.

Estimating the wave parameters is crucial for the wave mode identification and for understanding the role played by the waves in the Solar-Terrestrial interaction. Many of these parameters, such as the power spectral density, the coherency, the ellipticity, and the propagation direction can be determined using the magnetic field alone. Other parameters such as the Poynting vector and the phase relation between the magnetic field and the particle density, require additional measurements of other physical quantities.

Until the end of the mission, the four Cluster spacecraft altogether will gather the equivalent of close to one century of single spacecraft data from each instrument. Managing this amount of data poses challenges in computing, storing, and searching for relevant events. For instance, only obtaining the 2000 to 2018 ULF waves parameters discussed in the following sections required more than two months of continuous computing time on the eight threads of a 3.1 GHz Intel processor. A searchable archive of pre-computed ULF waves parameters has the potential to enable event-based and statistical studies otherwise difficult to conduct.

The multipoint capabilities of the Cluster fleet set it apart from most other spacecraft probing the Earth's magnetosphere and the solar wind. While even merely comparing the measurements from two spacecraft is useful in many investigations, more sophisticated techniques, such as the wave telescope/ $k$ -filtering (Glassmeier et al., 2001; Motschmann et al., 1996; Pinçon & Motschmann, 1998) or the curlometer (Dunlop et al., 2002) require specific shapes and sizes of the spacecraft formation, and their accuracy depends on the configuration parameters of the spacecraft tetrahedron. Even though computing these parameters is not as resource-demanding as computing the ULF waves parameters, a tool allowing quick estimation of the Cluster tetrahedron shape and size represents a useful instrument.

The remainder of this work is organized as follows: Section 2 discusses the derivation of the ULF waves parameters and provides the relations used to compute them later. Similarly, Section 3 discusses the tetrahedron configuration parameters. Section 4 is dedicated to the online Cluster Virtual Observatory (CVO) and describes in detail the archived data and the capabilities of the online tool. Section 5 summarizes this work. In addition, detailed descriptions of the content of the CVO is given in the Supporting Information S1 which accompanies this paper.

## 2. Derivation of the ULF Waves Parameters

Among the fundamental properties of the waves in magnetized plasma are the polarization parameters: the polarization degree, the ellipticity, and the orientation of the variance ellipsoid. These parameters can be determined based on the analysis of the spectral matrix obtained from the Fourier components corresponding to the analyzed frequency.

For a magnetic field  $\mathbf{B}$  with components  $B_i$ ,  $i = 1, \dots, 3$ , the spectral matrix elements in the measurement reference system are:

$$S_{ij}(\omega) = \langle \tilde{B}_i(\omega) \tilde{B}_j^*(\omega) \rangle \quad i, j = 1, \dots, 3 \quad (1)$$

where  $\langle \dots \rangle$  denotes the average and  $*$  denotes the complex conjugate.

The Fourier component

$$\tilde{B}_i(\omega) = \frac{1}{2\pi} \int B_i(t) e^{-i\omega t} dt \quad (2)$$

is approximated by the discrete Fourier transform usually by using the Fast Fourier Transform (FFT) method.

Note that if no averaging is performed in Equation 1, the spectral matrix is always singular and it is associated with a pure monochromatic plane wave with frequency  $\omega$ . In this case some of the wave parameters discussed in Section 2, such as the polarization degree Equation 12 or the coherency Equation 14, always take trivial values. Averaging includes the background waves by mixing neighboring spectral matrices and results in a spectral matrix characterizing the waves within a finite bandwidth around  $\omega$  instead of the idealized zero-bandwidth plane wave. Another benefit of averaging is the reduction of the statistical fluctuations of the spectral matrix estimate. The averaging can be done either in the time or in the frequency domain with equivalent results (Press et al., 1992, Ch. 13.4; Thomson & Emery, 2014, p. 436). For computing the spectral matrix used to derive the wave parameters saved in the CVO we average over frequency, as detailed in Section 4.1.1.

The methods for deriving the polarization parameters presented below are valid if at the analyzed frequency there is one dominant plane wave, that is, other waves—if present—have much smaller amplitudes. These smaller amplitude waves are treated as noise.

Arthur et al. (1976) discuss three methods which can be used to determine the polarization parameters of plasma waves. These three different approaches, briefly outlined below, yield similar but not identical results.

One of the methods, proposed by Samson (1973) decomposes the spectral matrices of  $n$ -variate processes into matrices directly connected to the polarization states. For  $n = 3$  the spectral matrix  $S$  is decomposed in three terms: one corresponding to the purely polarized part of the wave, one corresponding to the partial polarized part of the wave and one corresponding to the non polarized part of the wave. From this decomposition, the relative powers of the three polarization components of the wave result:

$$P_r = \frac{\lambda_1 - \lambda_2}{\Lambda}; \quad P_p = 2 \frac{\lambda_2 - \lambda_3}{\Lambda}; \quad P_N = 3 \frac{\lambda_3}{\Lambda} \quad (3)$$

where  $\lambda_1 \geq \lambda_2 \geq \lambda_3$  are the eigenvalues of the complex spectral matrix  $S$  in the measurement system and  $\Lambda = \lambda_1 + \lambda_2 + \lambda_3$ . In the proposed formalism, the  $n$ -dimensional degree of polarization is defined as

$$P_n^2 = \frac{1}{(n-1)(\text{tr}S)^2} \sum_{\substack{i,j=1 \\ i < j}}^n (\lambda_i - \lambda_j)^2 \quad (4)$$

Other wave parameters are then computed based on the spectral matrices associated with the different polarization states. The Samson (1973) method has the advantage of decomposing the data into quantities with clear physical meaning. One drawback which could become significant in the context of processing large quantities of data is the need of solving the eigenvalue problem for a complex matrix, which is more resource demanding than for a real matrix. Santolík et al. (2003) circumvents this problem by applying singular value decomposition (SVD) to the complex spectral matrix to derive many wave parameters. The SVD is much easier on resources and in addition the proposed method is generalized to naturally include the electric field vector, providing more information.

The other two methods discussed by Arthur et al. (1976) skip the decomposition into polarization states and directly transform the spectral matrix  $S$  from the measurement system into the principal system of the wave. In this reference system the wave vector is aligned with one of the axes. The varying magnetic field of the plane wave is therefore contained in the plane formed by the other two axes—the principal plane of the wave. One of the axes in this plane is aligned with the maximum variance direction of the magnetic field.

Consider an ideal plane wave of frequency  $\omega$  with the wave vector aligned with the  $z$ -axis.

$$B_x(t) = b_x e^{i\omega t} \quad (5a)$$

$$B_y(t) = b_y e^{i(\omega t - \pi/2)} \quad (5b)$$

$$B_z(t) = 0 \quad (5c)$$

The wave described by the above equations is already represented in its principal system. In this system the spectral matrix will be:

$$\mathcal{J} = \begin{pmatrix} b_x^2 & i b_x b_y & 0 \\ -i b_x b_y & b_y^2 & 0 \\ 0 & 0 & 0 \end{pmatrix} \quad (6)$$

If the measured wave departs from an ideal wave—which is always the case in practice—then a Hermitian matrix is added to  $\mathcal{J}$ . This additional matrix is interpreted as representing the noise. Note that only the  $2 \times 2$  upper left submatrix  $\mathcal{I}$  of  $\mathcal{J}$  is related with the plane wave. The third line and third column of  $\mathcal{J}$  are only related with the noise. The polarization parameters of the plane wave are extracted from the submatrix  $\mathcal{I}$ , which is composed from a diagonal real part  $\mathcal{I}'$  and an anti-symmetrical imaginary part  $\mathcal{I}''$ :

$$\mathcal{I} = \begin{pmatrix} b_x^2 & 0 \\ 0 & b_y^2 \end{pmatrix} + i b_x b_y \begin{pmatrix} 0 & 1 \\ -1 & 0 \end{pmatrix} = \mathcal{I}' + i\mathcal{I}'' \quad (7)$$

Note that the amplitudes of the two components of the wave can be recovered from the eigenvalues  $\lambda'_j = b_j^2$  of the real part  $\mathcal{I}'$ .

One way to find the wave principal system, discussed by Arthur et al. (1976) is based on the direct determination of the direction of the  $\mathbf{k}$  vector from the imaginary part  $S''$  of the spectral matrix  $S = S' + iS''$  in the measurement reference system (Means, 1972):

$$\hat{k}_l = (-1)^{l+1} S''_{mn} / q \quad l, m, n = 1, \dots, 3; \quad l \neq m \neq n; \quad m < n \quad (8)$$

where  $q^2 = \sum_{i,j=1}^3 (S''_{ij})^2$ . Note that the direction of the wave vector derived from Equation 8 corresponds to a right-hand polarized wave (with respect to the wave vector). If the wave is in fact left-hand polarized, then the true wave vector has the opposite direction.

Once the direction (up to the sign) of the wave vector is determined, the spectral matrix  $S$  is rotated in a coordinate system with the  $z$  axis along  $\hat{\mathbf{k}}$ . This is relatively easy to implement numerically and requires less CPU time than needed for the diagonalization of the spectral matrix. The result of this rotation is the spectral matrix  $\mathcal{H}$  in a reference system aligned with the wave vector but not yet aligned with the maximum variance direction. The transformation to the spectral matrix  $\mathcal{J}$  in the principal system of the wave requires an additional rotation around the  $z$  axis. The rotation angle is given by Rankin and Kurtz (1970):

$$\tan(2\phi) = \frac{2\Re(H_{xy})}{H_{xx} - H_{yy}} \quad (9)$$

One drawback of the Means (1972) method is that pure linearly polarized waves cannot be treated because in this case the spectral matrix  $S$  is real in any reference system, as can easily be checked in Equation 6.

The third technique considered by Arthur et al. (1976) was proposed by McPherron et al. (1972). In contrast with the Means (1972) method—which uses the imaginary part  $S''$  of the spectral matrix to find the transformation to the wave principal system—the McPherron et al. (1972) method implies the diagonalization of the real part  $S'$  of the spectral matrix. The rotation matrix  $\mathcal{T}$  from the measurement reference system to the principal system can be derived from the eigenvectors of  $S'$ :

$$\mathcal{T} = [\mathbf{v}'_1, \mathbf{v}'_2, \mathbf{v}'_3] \quad \lambda'_1 \geq \lambda'_2 \geq \lambda'_3 \quad (10)$$

The numerical implementation of the McPherron et al. (1972) method is relatively straightforward. The spectral matrix rotated into the principal system of the wave is:

$$\mathcal{J} = \mathcal{T}^T S \mathcal{T} \quad (11)$$

where  $^T$  denotes the transpose operation.

We use the spectral matrix rotated into the principal coordinates system Equation 11 for computing the wave parameters below. The wave vector direction used to determine the wave parameters in the database is given by the eigenvector  $\mathbf{v}'_3$  corresponding to the minimum eigenvalue of the real part of the spectral matrix. However, since the eigenvector  $\mathbf{v}'_3$  gives a direction which is either parallel or anti-parallel to the wave vector, we change the sign of  $\mathbf{v}'_3$  to agree with the sign of  $\hat{\mathbf{k}}$  from Equation 8, that is, to correspond to a right-hand polarized wave with respect to the wave vector.

The polarization degree is defined as the ratio between the wave coherent power and the total power of the wave (Fowler et al., 1967)

$$P^2 = 1 - 4 \frac{\det(\mathcal{I})}{(\text{tr} \mathcal{I})^2} \quad (12)$$

The above definition—adopted for the polarization degree stored in the CVO database—is identical to the degree of polarization Equation 4 for  $n = 2$ .

The ellipticity is defined as the ratio between the two axes of the polarization ellipsoid:

$$\epsilon = \tan \left[ \frac{1}{2} \arcsin \left( \frac{2\Im(I_{xy})}{\sqrt{(\text{tr} \mathcal{I})^2 - 4\det(\mathcal{I})}} \right) \right] \quad (13)$$

with the sign determined by the sign of  $\mathbf{k} \cdot \mathbf{B}$  with  $\mathbf{k}$  derived from Equation 8.

The coherency is defined using the spectral matrix elements (Rankin & Kurtz, 1970):

$$\gamma = \frac{|I_{xy}|^2}{I_{xx}I_{yy}} \quad (14)$$

If assuming incoherent isotropic noise, the intensity of the coherent part of the wave (Song & Russell, 1999) is

$$I_{\text{coh}} = \lambda'_1 + \lambda'_2 - 2\lambda'_3 \quad (15)$$

Any wave can be decomposed into a sum of left hand polarized and right hand polarized waves (Kodera et al., 1977; Song & Russell, 1999).

Under the assumption of large signal-to-noise ratio ( $\lambda'_3 \ll \lambda'_1 + \lambda'_2$ ), the amplitudes of the right hand and of the left hand polarized components are given by:

$$A_{\pm} = \frac{\sqrt{\lambda'_1 - \lambda'_3}}{2}(1 \pm \epsilon) \quad (16)$$

From these, the amplitudes of the linearly polarized part of the wave and the amplitude of the circularly polarized part of the wave can be determined.

$$A_{\text{lin}} = \sqrt{2A_+A_-} \quad (17)$$

$$A_{\text{circ}} = \sqrt{|A_+^2 - A_-^2|} \quad (18)$$

Another important wave parameter determined using the magnetic field alone is the compression ratio, that is, the ratio between the power spectral density of the oscillations parallel to the mean magnetic field and the total power spectral density. In a coordinate system with the  $z$  axis aligned with the mean magnetic field, the compression ratio is

$$C = \frac{\rho_z}{\rho_x + \rho_y + \rho_z} \quad (19)$$

where  $\rho_j = \langle |\tilde{B}_j|^2 \rangle$  is the power spectral density of the component  $j$  in the mean-field aligned coordinate system. Note that the parameter saved in the database is  $1 - C$ .

All the parameters discussed above are derived solely from the magnetic field. However, the time varying magnetic field of the waves propagating into the plasma is coupled with the electric field, and in addition the waves also disturb and are influenced by the plasma particle distributions. In particular, the coupling between the magnetic field magnitude and the particle density is important in the analyzing of plasma waves. One useful quantity in this respect is the cross-spectral matrix of the magnetic field and particle density:

$$\mathcal{G}_{Bn}(\omega) = \langle \tilde{\mathbf{B}}(\omega) \tilde{n}^*(\omega) \rangle \quad (20)$$

where  $\tilde{\mathbf{B}}$  is the Fourier transform of the magnetic field modulus and  $\tilde{n}$  is the Fourier transform of the particle density.

From the cross-spectral matrix, a number of fundamental quantities characterizing the relation between the  $B(t)$  and  $n(t)$  can be derived. One of the most important is the phase shift between  $B$  and  $n$ :

$$\varphi_{Bn} = \arg(\mathcal{G}_{Bn}) \quad (21)$$

The coherency between  $B(t)$  and  $n(t)$  is given by:

$$\gamma_{Bn}(\omega) = \frac{|\mathcal{G}_{Bn}|^2}{\mathcal{G}_{BB}\mathcal{G}_{nn}} \quad (22)$$

The co-spectrum, equal to the real part of the off-diagonal elements,  $\Re(\mathcal{G}_{Bn})$ , represents the in-phase and opposite-phase part of the signals. The quad-spectrum, equal to the imaginary part of the off-diagonal elements,

$\Im(G_{Bn})$ , represents phase-quadrature ( $\pm\pi/2$  phase difference, advanced/retarded) part of the signals (Jenkins & Watts, 1968, p. 343).

Finally, a key parameter of the ULF waves is the Poynting vector which provides the electromagnetic energy flux:

$$\mathbf{S}(\omega) = \frac{1}{2\mu_0} \Re(\tilde{\mathbf{E}} \times \tilde{\mathbf{B}}^*) \quad (23)$$

Knowledge of the Poynting vector supports the identification of stationary waves, and of energy source and sink regions.

### 3. Derivation of the Configuration Parameters

All multipoint data analyzing techniques depend on the geometric properties of the sensor network. The minimum number of measuring points required for deriving three dimensional quantities and to differentiate between spatial and temporal fluctuations is four, the number of spacecraft in the Cluster fleet. However, not any configuration of four spacecraft is appropriate for three dimensional analysis. The dimensionality is reduced to 2 if all spacecraft are contained in a plane and to 1 if they are aligned along a line. To characterize the configurations lying in between these extremes one may use the elongation and planarity parameters derived from the volumetric tensor which is defined as (Robert et al., 1998b):

$$R_{ij} = \frac{1}{N} \sum_{\alpha=1}^N r_i^\alpha r_j^\alpha \quad (24)$$

where  $r_k^\alpha$  is the component  $k$  of the position vector  $\mathbf{r}^\alpha$  of spacecraft  $\alpha$  relative to the barycentre of the formation,  $\sum_{\alpha=1}^N \mathbf{r}^\alpha = 0$ .

The characteristic dimensions of the tetrahedron are given by the eigenvalues of the volumetric tensor  $\mathcal{R}$ , while the eigenvectors give the orientation of the volumetric ellipsoid. For Cluster,  $N = 4$  and the volume of the tetrahedron is given by the determinant of the volumetric tensor  $V = (8/3)\sqrt{|\mathcal{R}|}$ . Therefore when  $|\mathcal{R}| = 0$ , the formation is either flattened into a 2D plane or elongated into a 1D line.

If  $a_1 \geq a_2 \geq a_3$  are the eigenvalues, and  $\mathbf{R}_1, \mathbf{R}_2, \mathbf{R}_3$  are the corresponding eigenvectors of the volumetric tensor  $\mathcal{R}$ , the elongation is defined as

$$e = 1 - \sqrt{\frac{a_2}{a_1}} \quad (25)$$

with the direction given by the eigenvector  $\mathbf{R}_1$  corresponding to the maximum eigenvalue. When the elongation approaches 0, the spacecraft tend to be equally distanced from each other, when the elongation approaches 1, the tetrahedron shape degenerates to a string.

The planarity is defined as

$$p = 1 - \sqrt{\frac{a_3}{a_2}} \quad (26)$$

with the normal to the flattening given by the eigenvector  $\mathbf{R}_3$  corresponding to the minimum eigenvalue. When the planarity approaches 1, all spacecraft are contained in a plane.

The pair  $(e, p)$  gives the shape of the formation and determines its dimensionality which is of key importance for multi-spacecraft analysis methods.

The size of the constellation also matters. The characteristic size of the tetrahedron is the largest dimension of the volumetric ellipsoid

$$L = 2\sqrt{a_1} \quad (27)$$

If the distances between the spacecraft are larger than the correlation length of the phenomenon being studied, then the measurements become just a collection of unrelated single point measurements and can be combined

only in a statistical sense. Within the correlation length, if the distances between spacecraft are larger than the wavelength/scale of the phenomenon being investigated, spatial aliasing will occur (Sahraoui et al., 2010). If the distances between the spacecraft become too small compared with the scale of the phenomenon being studied, then the measurements become identical and the constellation becomes equivalent with a single point measurement.

#### 4. The Online Virtual Observatory

The almost two solar cycles covered by the Cluster multipoint magnetospheric measurements are a valuable resource offering opportunities for unprecedented statistical studies, as well as for case studies of common phenomena in extreme or unusual conditions. For the study of plasma waves over individual time intervals one could use dedicated analyzing tools such as PRASSADCO (Cornilleau-Wehrin et al., 2005) to compute and visualize the key waves parameters. However, the sheer size of the data collected by Cluster over two decades poses new challenges in managing and filtering the data. This is why a database containing high level data is essential to make these studies possible. The parameters of the ULF waves discussed in Section 2 are among the best candidates for such database.

To take full advantage of the multipoint measurements offered by Cluster, one must employ specialized multipoint techniques, such as the curlometer (Dunlop et al., 2002; Robert et al., 1998a) or the wave telescope (Glassmeier et al., 2001) which can only be applied for specific geometric configurations of the Cluster tetrahedron. The plots of the configuration parameters on the CVO website allow for a quick estimation of the quality and size of the configuration, linked with the position in GSE.

##### 4.1. ULF Waves Parameters

Using measurements of the magnetic field  $B$ , the electric field  $E$  and the plasma density  $n$ , 47 parameters characterizing the ULF waves are computed, saved in the database and plotted to enable quick browsing. A list of the computed parameters can be found in Tables S1 and S2 in the accompanying Supporting Information S1. It is important to note that the parameters are computed in the spacecraft frame, without any Doppler correction.

###### 4.1.1. Data Analysis

The magnetic field data measured by the FGM as well as the electric field and the spacecraft potential measured by the Electric Field and Wave Experiment (EFW) (Gustafsson et al., 1997) are obtained from the ESA *Cluster Science Archive* (CSA) (<https://cosmos.esa.int/web/csa>).

Before computing the ULF waves parameters, the magnetic field data is preprocessed to identify data gaps and bad data, and resampled to a rate of one vector per second. When available, high resolution (25 or 450 vect/s) electric field data are downloaded from the CSA. These are also resampled to one vector per second and synchronized with the magnetic field data. For the time intervals without high resolution electric field data available, low resolution data (one vector per 4 s) is used. In this case the resulting frequency domain is more restricted. The electron density is obtained from the spacecraft potential following Lybekk et al. (2012). The advantage over using the density delivered by the dedicated particle instruments is the much higher temporal resolution and data availability.

All the parameters are computed in the time frequency domain using (directly or indirectly) a sliding window of 2,048 s (34 min and 8 s). The sliding step of 256 s (4 min and 16 s) is one eighth of the window length. For a 24 hr interval, 338 evaluations are thus performed on the time axis. A sampling rate of one Hz results in a Nyquist frequency of 0.5 Hz. The frequency resolution from the *FFT* method is equal to the inverse of the window length (0.48 mHz), while the number of frequencies for which each parameter is computed is equal to half of the window size plus one (1,025 frequencies). Therefore, for a 1 day interval of data, each parameter is computed for each cell of a  $338 \times 1,025$  domain in the time-frequency space. The background magnetic field was computed as the average over the sliding window.

For computing the spectral matrix Equation 1, central to the derivation of many wave parameters, we first de-trend the data in the analyzing window, we taper the de-trended data using a Hanning window (normalized to preserve the power) and then we apply a FFT to the result.

We choose to perform a five points boxcar (two points to the left and two points to the right) average over frequency domain. One side effect of the averaging is the reduction of the frequency resolution from 0.48 to 2.4 mHz. Since most of the ULF waves below 0.5 Hz typically cover a much broader frequency band, this is not a significant drawback.

The computed parameters are valid only under certain conditions. For instance, all the parameters involving the magnetic field lose their validity when the magnetic field variations decrease towards the noise level. A binary mask based on the power spectral density is constructed to mark the invalid time-frequency regions. Similarly, binary masks are constructed based on the power spectral densities (PSDs) of the electric field and of the Poynting vector, on the polarization degree, on the spectral matrix eigenvalues ratio, on the coherency between the magnetic field and the density variations, and on the angle between the wave vector and the mean magnetic field direction. Not all masks are applied to all parameters, for instance, the last mask ( $\widehat{k\mathbf{B}}$ ) is only used to mark as bad the computed ellipticity when the wave vector is nearly orthogonal to the mean magnetic field. The masks are saved together with the computed parameters and are used to remove the bad values from the plots.

#### 4.1.2. Plots Archive

The heart of the ULF Observatory is the browsable archive of plots representing the wave parameters as daily spectrograms. While all parameters enumerated in Tables S1 and S2 in Supporting Information S1 are saved in the data archive, only a subset of them are part of the plots archive. The plots are organized into six sets of seven parameters each. To facilitate visual analysis, the first panel for all plot sets shows the time series of the magnetic field together with condensed information about the orbit. In addition, the magnetospheric regions crossed by the spacecraft and the location of the magnetic foot points when the spacecraft orbit intersects closed field lines are encoded by horizontal colored bars. The information about the magnetospheric regions and foot points is obtained from the Goddard SSCWeb interface <http://sscweb.gsfc.nasa.gov> using IGRF internal and Tsyganenko 89C external model and is only meant as a rough guide. Many parameters appear in multiple sets, therefore the total number of distinct parameters in the plots archive is 29. We briefly describe below the default parameter set in the plots archive. The other five sets are shown and discussed in the Supporting Information S1.

The basic parameters set is illustrated in Figure 1. The top panel shows the time series for the three components of the magnetic field in GSE coordinates. The plotted magnetic field is high-pass filtered to exclude periods longer than the analyzing window (2,048 s). To differentiate between the three components, an offset of 5 nT is added to the  $x$  component and subtracted from the  $y$  component. The three insets on the left show the projections of the spacecraft orbit on the GSE ( $x, z$ ), ( $y, z$ ), and ( $x, y$ ) planes with the starting point marked by the magenta circle. The colored bar at the top of the panel indicates the magnetospheric regions crossed by the spacecraft according to Tsyganenko 89C (Tsyganenko, 1989) with  $K_p = 3$ , in this case dayside magnetosheath during the entire interval. Because of departures of the actual  $K_p$  index from the constant index used, and because of the dynamics of the magnetospheric boundaries, one can clearly see from the data that in fact the spacecraft finds itself in the solar wind at the beginning of the interval and the bowshock moves back and forth several times until the spacecraft moves deeper into the magnetosheath. If the spacecraft reaches further into the magnetosphere into the closed field lines region, then the foot points in the northern and southern hemisphere would be indicated by two colored bars stacked at the bottom of the panel, not present in this figure, but visible in Figure S10 in Supporting Information S1 showing the web interface.

For the first parameter in the set, plotted in panel (b), we use the spectral matrix to compute the total power spectral density of the magnetic field fluctuations, defined as the sum of the PSDs of the three GSE components. The gyrofrequencies of the H, He, O, and O<sub>2</sub> computed from the magnetic field smoothed using a boxcar average of 1,024 s are plotted on top of the spectrogram with white solid, dotted and again solid and dotted lines, respectively. The position of the spacecraft relative to the GSE ( $x, y$ ) (equatorial) and ( $x, z$ ) (noon-midnight meridian plane) planes is marked at the top of this panel by colored bars as follows: Red if the angle between the position vector and the equatorial plane is less than 10°. Yellow if the angle between the position vector and the noon-midnight meridian plane is less than 10° and the  $x$  coordinate is positive (dayside). Green if the angle between the position vector and the noon-midnight meridian plane is less than 10° and the  $x$  coordinate is negative (nightside). If both the equatorial plane angle and the noon-midnight angle are below 10° then two color bars are visible. The color convention is summarized in Table 1. None of these conditions occurred during 20th May 2005 therefore no colored bars are present in Figure 1 PSD panel. Figure S10 in Supporting Information S1 shows an example when the spacecraft orbit intersects both planes.

The next two panels (c, d) show the orientation of the wave vector  $\mathbf{k}$  Equation 8 as given by the azimuth  $\varphi$  and by the elevation  $\theta$  angles in GSE coordinates. Since the sign of the wave vector  $\mathbf{k}$  is not determined, we changed the

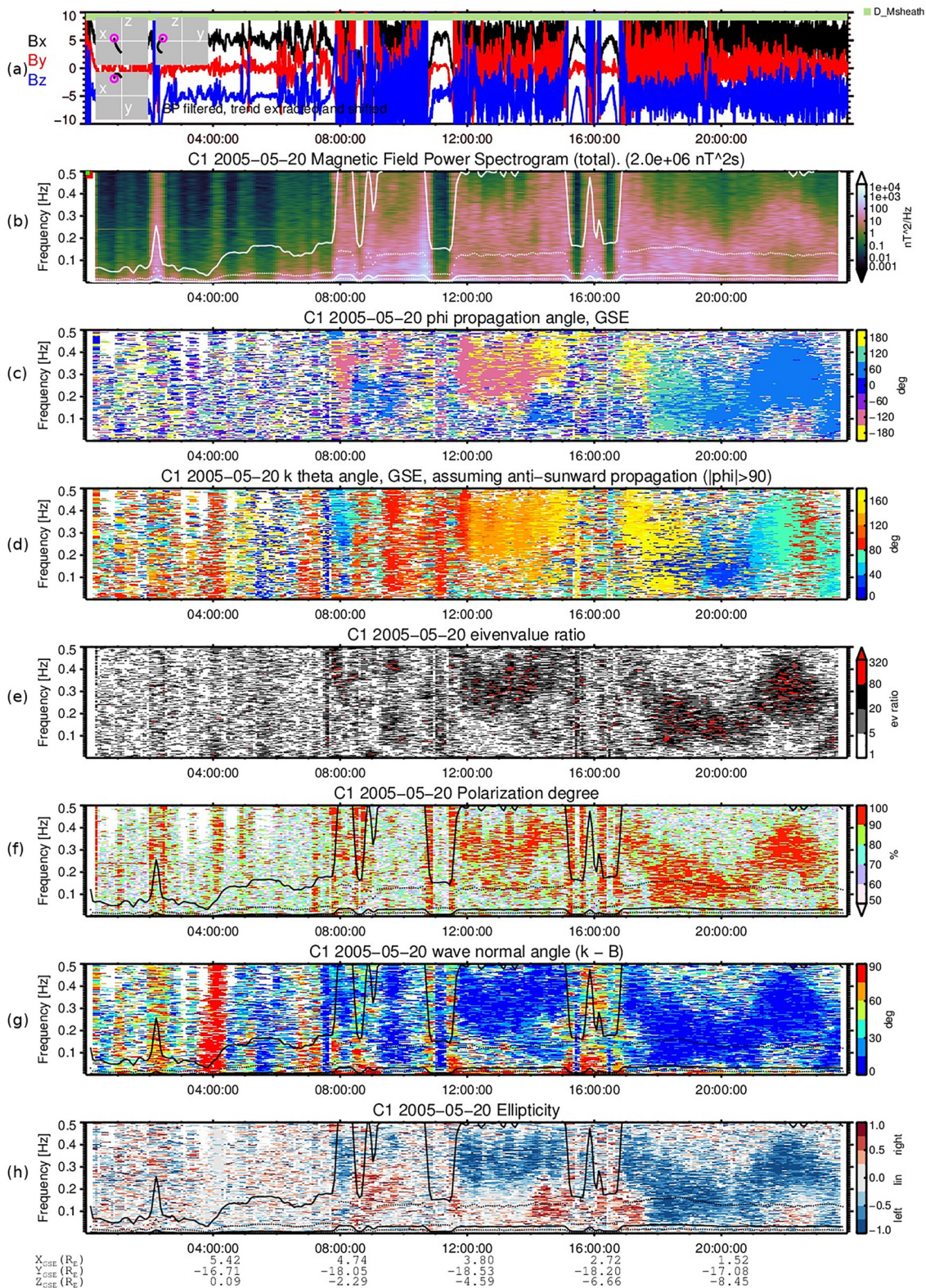


**Figure 1.** The basic parameters plot set for Cluster 1 on 20 May 2005. From top to bottom: (a) The GSE components of the magnetic field, high-pass filtered. The insets show the orbit in GSE, the top bar shows the magnetospheric region; (b) The sum of the power spectral densities of the magnetic field components. The white lines show the gyrofrequencies of H, He, O, and O<sub>2</sub>; (c, d) The azimuth and elevation angles of the wave vector in GSE; (e) The ratio between the intermediate and the minimum eigenvalue; (f) The polarization degree; (g) The angle between the wave vector and the mean magnetic field; and (h) The ellipticity.

**Table 1**  
Color Convention for Marking the Spacecraft Position in the Plots

Color	Position	Condition
Red	Equatorial plane	$ \arcsin(r_z/r)  < 10^\circ$
Yellow	Dayside	$ \arcsin(r_y/r)  < 10^\circ$ $r_x > 0$
Green	Nightside	$ \arcsin(r_y/r)  < 10^\circ$ $r_x < 0$

elevation angle to correspond to anti-sunward propagation ( $|\phi| \leq 90$ ). While at the beginning of the interval the propagation direction of the waves seems to be random, later in the day there are clear time-frequency “islands” where the waves propagate along a stable direction.

To remove from the plot low power fluctuations we discarded the time-frequency cells corresponding to total PSD less than  $5 \times 10^{-3} \text{ nT}^2 \text{ Hz}^{-1}$ . We applied this power mask to all parameters derived from the magnetic field, except the other PSDs. Moreover, to reduce the noise in the plot we discarded the time-frequency cells corresponding to polarization degree

below 70%. Finally, because a low eigenvalue ratio leads to large errors in the determined wave vector direction we also discarded the time-frequency cells corresponding to intermediate to minimum eigenvalue ratios less than 5.

The ratio between the intermediate and the minimum eigenvalues of the spectral matrix Equation 1 plotted in panel (e) provides useful information about how well the wave propagation direction is defined. This relates to the assumption of dominant plane wave made in Section 2. A high eigenvalue ratio signifies that the plane wave assumption is correct. To properly represent the range of eigenvalue ratios we use a logarithmic base 4 representation. All cells below the threshold ratio (equal to 5) are masked out (white) and all values above 80 are plotted with red. Other masks applied: PSD.

The polarization degree Equation 12 is shown in panel (f). Only the PSD mask is applied here. Note that the high polarization domain resembles the large eigenvalue ratio domain in the previous panel. Here and in the next two panels the gyrofrequencies of H, He, O, and O<sub>2</sub> are plotted with black lines on top of the spectrogram.

Panel (g) shows the wave normal angle, that is, the angle between the wave vector and the mean magnetic field computed over the window length  $W$ . Because of the sign uncertainty we reduced the angles to the  $[0^\circ, 90^\circ]$  interval. For this panel we applied the masks for PSD, polarization degree and eigenvalue ratios with the thresholds mentioned above. One can see that during this day most of the waves with high polarization and power in the magnetosheath propagate either parallel or anti-parallel to the mean magnetic field. In front of the magnetosheath the waves do not seem to have a preferred direction with the exception of a short time interval around 04:00 UT when the wave vector is orthogonal to the magnetic field for all frequencies.

The last panel (h) in this set shows the waves ellipticity Equation 13. For this panel we applied the same masks as for the wave normal angle. In addition we masked out the time-frequency cells with near orthogonal propagation ( $\alpha_{kB} \geq 80^\circ$ ) because for orthogonal propagation the ellipticity is undefined. Most of the parallel propagating waves are circularly polarized to the left with some exceptions in the lower frequency range close to the bowshock crossings when the polarization is to the right. In front of the bowshock no preferred ellipticity is observed with the exception of the waves around 04:00 UT showing linear polarization.

#### 4.1.3. Data Archive

The daily  $338 \times 1,025$  time-frequency matrix for each parameter is saved using the *Hierarchical Data Format* (HDF) standard (Poinot, 2010), together with a low resolution plot for quick reference. The corresponding time and frequency vectors, details on how the parameter was computed, the reference system, and the units used are saved as well in the same HDF file. The total size of the archived parameters is over 2 TB. At the moment there is no query capability implemented, but the data can be downloaded and then locally processed.

A subset of the low resolution plots meant for quick visual inspection of the database content are presented in the Supporting Information S1. To avoid obscuring potential significant features, no masks are applied, therefore one should exercise caution when interpreting these plots.

#### 4.2. Configuration Parameters

The configuration parameters characterize the shape and the size of the Cluster tetrahedron. They are essential for determining the applicability and for the error evaluation of multi-point analysis techniques. In Section 3 we introduced the elongation and the planarity which condense the shape information for a tetrahedron in an intuitive fashion. Since both can only take values between 0 and 1, any tetrahedron shape corresponds to one point in the unit square of the elongation-planarity diagram. Table 2 summarizes the possible shapes in the  $(e, p)$  space.

**Table 2**  
*Shapes in the Planarity-Elongation Domain*

Planarity	Elongation				
	0	Low	Intermediate	Large	1
1	Circle	Ellipse	Ellipse	Ellipse	Line
Large	Lens	Pancake	Elongated pancake	Knife blade	Line
Intermediate	Lens	Thick pancake	Potato	Flat cigar	Line
Low	Lens	Egg	Short cigar	Cigar	Line
0	Sphere	Rugby ball	Rugby ball	Rugby ball	Line

*Note.* Adapted from Robert et al. (1998b).

Note that the configuration parameters can also be obtained directly from the CSA. However, the graphical representations presented here allow for a quick inspection of these parameters, from multi-year overviews to daily plots with below 1 hr detail.

For a long term overview of the configuration parameters of the Cluster tetrahedron we produced plots such as the one shown in Figure 2. Each plot consists of four panels, each panel showing the mean inter-spacecraft distance during 1 year. The shape of the formation is encoded in the color of the plot line, with a color-key in the upper right corner. The color-key is a representation of the  $(e, p)$  space, with the origin  $(0, 0)$  at the lower left corner, and maximum value  $(1, 1)$  at the upper right corner. The red color near origin indicates a nearly regular tetrahedron. The yellow color (large elongation, low planarity) indicates cigar shapes. The green color indicates shapes resembling a long, flat knife blade. The blue color indicates nearly circular flattened pancake shaped formations. The gray color in the center indicates irregular “potato” shapes. The function chosen to map the  $(e, p)$  space to the  $(r, g, b)$  space is bijective, therefore one can estimate the shape of the tetrahedron at a given moment in time from the color of the corresponding line in the plot.

Yearly, monthly and daily plots are also provided. Detailed descriptions and example plots are included in the Supporting Information S1.

### 4.3. The Web Interface

The CVO for ULF waves is organized into three main sections. The *ULF quickplots* (Figure S10 in Supporting Information S1, <http://plasma.space-science.ro/waves/index.html>) section offers access to the plots archive discussed in Section 4.1.2. The spacecraft, date, and plot set can be selected using the buttons above the image. Below the image, there are links to high resolution JPG or pdf formats of the plots, to a catalog containing the plots for the entire year, and to a text file with details about how the plots were produced. This text file is embedded both in the JPG image header and in the pdf file.

The *ULF data* (Figure S11 in Supporting Information S1, <http://plasma.space-science.ro/waves/spectra-data/>) section provides access to the ULF waves parameters data archive discussed in Section 4.1.3. The spacecraft, year, month and parameter are selected using the buttons at the top of the page. The “go” button displays the low resolution images of the selected parameter for the selected month together with links to the HDF files containing the archived data. If many data files are necessary, they can be downloaded by resorting to common web programs—such as `lftp` or `wget`. The web root of the database is <http://plasma.space-science.ro/waves/spectra-data/Fourier/>. From here, the datafile corresponding the parameter `ParamName` from the spacecraft `CN` on the date `YYYY-MM-DD` can be found under `CN/YYYY/ParamName/CN_ParamName_YYYY-MM-DD.hdf`.

The *Tetrahedron geometry* (Figure S12 in Supporting Information S1, <http://plasma.space-science.ro/waves/geometry.html>) section offers access to the plots of the configuration parameters of the Cluster fleet discussed in Section 4.2. From the buttons at the top of the page, the desired plot can be selected and displayed. Links to high resolution JPG and pdf files as well as to a yearly catalog are provided at the bottom of the page.

## 5. Summary and Conclusions

The large volume of data accumulated by the Cluster mission in the last two decades is both a valuable resource and a challenge to digest in an efficient manner. The many parameters characterizing the low frequency plasma

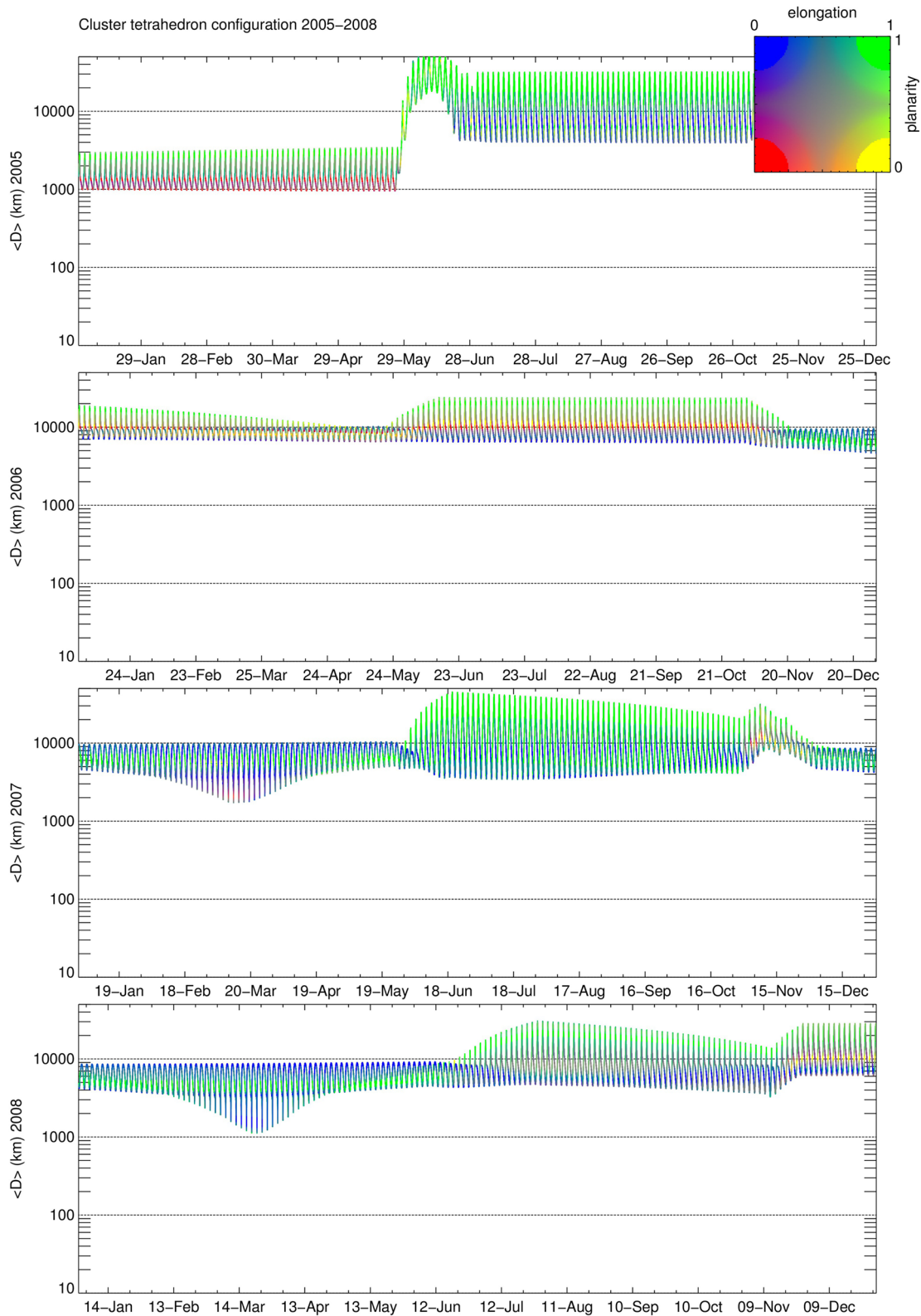


**Figure 2.** Configuration parameters of the Cluster tetrahedron between 2005 and 2008. The y axis shows the mean inter-spacecraft distance and the color encodes the tetrahedron shape in the  $(e, p)$  domain as given by the color legend in the upper right. Red color denotes nearly regular configuration, blue denotes a flat configuration with approximately equal distances between the spacecraft, green and yellow denote string of pearls configurations.

waves are a good example of high level data whose availability have the potential to significantly reduce the effort needed to select relevant events or to conduct large statistical studies. If multipoint analyses are performed, a possibility to quickly find appropriate spacecraft configurations is highly desirable as well. The CVO offers both the high level ULF waves parameters and an optimized interface to graphical representations of the spacecraft configuration. A browsable database of daily plots of the ULF waves parameters allows for a rapid search for significant events and provides publication quality images. The main data used to build the CVO database is the magnetic field delivered by the Cluster FGM instruments. Additionally, the spacecraft potential and the electric field from the EFW instrument are used to compute specific parameters. For a rough positioning within the magnetospheric regions, data from the Goddard SSCWeb is utilized. The CVO can be accessed without restrictions at <http://plasma.space-science.ro/cluster.html>.

## Data Availability Statement

Data sets used for this work are available from the ESA *Cluster Science Archive* (ESA, 2023; Masson et al., 2014) and from the NASA *Goddard Satellite Situation Center Web* (NASA, 2023).

## References

- Arthur, C. W., McPherron, R. L., & Means, J. D. (1976). A comparative study of three techniques for using the spectral matrix in wave analysis. *Radio Science*, 11(10), 833–845. <https://doi.org/10.1029/RS011i010p00833>
- Balogh, A., Dunlop, M. W., Cowley, S. W. H., Southwood, D. J., Thomlinson, J. G., Glassmeier, K. H., et al. (1997). The cluster magnetic field investigation. *Space Science Reviews*, 79(1/2), 65–91. <https://doi.org/10.1023/A:1004970907748>
- Cornilleau-Wehrin, N., Alleyne, H. S., Yearby, K. H., de la Porte de Vaux, B., Meyer, A., Santolík, O., et al. (2005). The STAFF-DWP wave instrument on the DSP equatorial spacecraft: Description and first results. *Annales Geophysicae*, 23(8), 2785–2801. <https://doi.org/10.5194/angeo-23-2785-2005>
- Cornilleau-Wehrin, N., Chauveau, P., Louis, S., Meyer, A., Nappa, J. M., Perraut, S., et al. (1997). The cluster spatio-temporal analysis of field fluctuations (STAFF) experiment. *Space Science Reviews*, 79(1/2), 107–136. <https://doi.org/10.1023/A:1004979209565>
- Dunlop, M. W., Balogh, A., Glassmeier, K. H., & Robert, P. (2002). Four-point Cluster application of magnetic field analysis tools: The Curlometer. *Journal of Geophysical Research*, 107(A11), 1384. <https://doi.org/10.1029/2001JA005088>
- ESA. (2023). Cluster and double star science archive. Retrieved from <https://cosmos.esa.int/web/csa>
- Escoubet, C. P., Schmidt, R., & Goldstein, M. L. (1997). Cluster: Science and mission overview. *Space Science Reviews*, 79(1/2), 11–32. <https://doi.org/10.1023/A:1004923124586>
- Fowler, R., Kotick, B., & Elliott, R. (1967). Polarization analysis of natural and artificially induced geomagnetic micropulsations. *Journal of Geophysical Research*, 72(11), 2871–2883. <https://doi.org/10.1029/JZ072i011p02871>
- Glassmeier, K.-H. (1995). ULF pulsations. In H. Volland (Ed.), *Handbook of atmospheric electrodynamics* (pp. 463–502). CRC Press.
- Glassmeier, K.-H., Motschmann, U., Dunlop, M., Balogh, A., Acuña, M. H., Carr, C., et al. (2001). Cluster as a wave telescope - First results from the fluxgate magnetometer. *Annales Geophysicae*, 19(10/12), 1439–1447. <https://doi.org/10.5194/angeo-19-1439-2001>
- Gustafsson, G., Bostrom, R., Holback, B., Holmgren, G., Lundgren, A., Stasiewicz, K., et al. (1997). The electric field and wave experiment for the cluster mission. *Space Science Reviews*, 79(1/2), 137–156. <https://doi.org/10.1023/A:1004975108657>
- Jenkins, G. M., & Watts, D. G. (1968). Spectral analysis and its applications.
- Keiling, A., Lee, D., & Nakariakov, V. (Eds.). (2016). *Low frequency waves in space plasmas*. American Geophysical Union. <https://doi.org/10.1002/9781119055006>
- Kodera, K., Gendrin, R., & de Villedary, C. (1977). Complex representation of a polarized signal and its application to the analysis of ULF waves. *Journal of Geophysical Research*, 82(7), 1245–1255. <https://doi.org/10.1029/JA082i007p01245>
- Lemmens, S., Merz, K., & Funke, Q. (2017). Planned yet uncontrolled re-entries of the Cluster-II spacecraft. In T. Flohrer & F. Schmitz (Eds.), *7th european conference on space debris* (Vol. 7). ESA Space Debris Office.
- Lybekk, B., Pedersen, A., Haaland, S., Svensen, K., Fazakerley, A. N., Masson, A., et al. (2012). Solar cycle variations of the cluster spacecraft potential and its use for electron density estimations. *Journal of Geophysical Research*, 117(A1), A01217. <https://doi.org/10.1029/2011JA016969>
- Masson, A., Escoubet, C. P., & Laakso, H. (2014). Cluster science archive: The ESA long term archive of the cluster mission. In *Egu general assembly conference abstracts* (p. 7422).
- McPherron, R. L., Russell, C. T., & Coleman, P. J., Jr. (1972). Fluctuating magnetic fields in the magnetosphere. II: ULF waves. *Space Science Reviews*, 13(3), 411–454. <https://doi.org/10.1007/BF00219165>
- Means, J. D. (1972). Use of the three-dimensional covariance matrix in analyzing the polarization properties of plane waves. *Journal of Geophysical Research*, 77(28), 5551–5559. <https://doi.org/10.1029/JA077i028p05551>
- Motschmann, U., Woodward, T. I., Glassmeier, K. H., Southwood, D. J., & Pinçon, J. L. (1996). Wavelength and direction filtering by magnetic measurements at satellite arrays: Generalized minimum variance analysis. *Journal of Geophysical Research*, 101(A3), 4961–4966. <https://doi.org/10.1029/95JA03471>
- NASA. (2023). Satellite situation center web. Retrieved from <http://sscweb.gsfc.nasa.gov>
- Pilipenko, V. A. (1990). ULF waves on the ground and in space. *Journal of Atmospheric and Terrestrial Physics*, 52(12), 1193–1209. [https://doi.org/10.1016/0021-9169\(90\)90087-4](https://doi.org/10.1016/0021-9169(90)90087-4)
- Pinçon, J., & Motschmann, U. (1998). Multi-spacecraft filtering: General framework. In G. Paschmann & P. Daly (Eds.), *Analysis methods for multi-spacecraft data* (pp. 65–78). ISSI.
- Pointot, M. (2010). Five good reasons to use the hierarchical data format. *Computing in Science & Engineering*, 12(5), 84–90. <https://doi.org/10.1109/MCSE.2010.107>
- Press, W. H., Flannery, B. P., Teukolsky, S. A., & Vetterling, W. T. (1992). *Numerical recipes in Fortran 77: The art of scientific computing*. Cambridge University Press.

- Rankin, D., & Kurtz, R. (1970). Statistical study of micropulsation polarizations. *Journal of Geophysical Research*, 75(28), 5444–5458. <https://doi.org/10.1029/JA075i028p05444>
- Robert, P., Dunlop, M. W., Roux, A., & Chanteur, G. (1998a). Accuracy of current density determination. *ISSI Scientific Reports Series, 1*, 395–418.
- Robert, P., Roux, A., Harvey, C. C., Dunlop, M. W., Daly, P. W., & Glassmeier, K.-H. (1998b). Tetrahedron geometric factors. *ISSI Scientific Reports Series, 1*, 323–348.
- Sahraoui, F., Belmont, G., Goldstein, M. L., & Rezeau, L. (2010). Limitations of multispacecraft data techniques in measuring wave number spectra of space plasma turbulence. *Journal of Geophysical Research*, 115(A4), A04206. <https://doi.org/10.1029/2009JA014724>
- Samson, J. C. (1973). Descriptions of the polarization states of vector processes: Applications to ULF magnetic fields. *Geophysical Journal International*, 34(4), 403–419. <https://doi.org/10.1111/j.1365-246X.1973.tb02404.x>
- Santolík, O., Parrot, M., & Lefeuvre, F. (2003). Singular value decomposition methods for wave propagation analysis. *Radio Science*, 38(1), 1010. <https://doi.org/10.1029/2000RS002523>
- Song, P., & Russell, C. T. (1999). Time series data analyses in space physics. *Space Science Reviews*, 87(3/4), 387–463. <https://doi.org/10.1023/A:1005035800454>
- Thomson, R., & Emery, W. (2014). *Data analysis methods in physical oceanography*. Elsevier Science.
- Tsyganenko, N. A. (1989). A magnetospheric magnetic field model with a warped tail current sheet. *Planetary and Space Science*, 37(1), 5–20. [https://doi.org/10.1016/0032-0633\(89\)90066-4](https://doi.org/10.1016/0032-0633(89)90066-4)